PHYSICAL REVIEW D **78,** 123523 (2008)

# Nonlinear evolution of $f(R)$ cosmologies. I. Methodology

Hiroaki Oyaizu*

*Department of Astronomy and Astrophysics, University of Chicago, Chicago, Illinois 60637, USA;*
*Kavli Institute for Cosmological Physics, University of Chicago, Chicago, Illinois 60637, USA*
(Received 17 July 2008; published 18 December 2008)

We introduce the method and the implementation of a cosmological simulation of a class of metric-variation $f(R)$ models that accelerate the cosmological expansion without a cosmological constant and evade solar-system bounds of small-field deviations to general relativity. Such simulations are shown to reduce to solving a nonlinear Poisson equation for the scalar degree of freedom introduced by the $f(R)$ modifications. We detail the method to efficiently solve the nonlinear Poisson equation by using a Newton-Gauss-Seidel relaxation scheme coupled with the multigrid method to accelerate the convergence. The simulations are shown to satisfy tests comparing the simulated outcome to analytical solutions for simple situations, and the dynamics of the simulations are tested with orbital and Zeldovich collapse tests. Finally, we present several static and dynamical simulations using realistic cosmological parameters to highlight the differences between standard physics and $f(R)$ physics. In general, we find that the $f(R)$ modifications result in stronger gravitational attraction that enhances the dark matter power spectrum by $\sim$20% for large but observationally allowed $f(R)$ modifications. A more detailed study of the nonlinear $f(R)$ effects on the power spectrum are presented in a companion paper.

DOI: 10.1103/PhysRevD.78.123523 PACS numbers: 98.80.−k, 04.50.Kd

## I. INTRODUCTION

Explaining the accelerated cosmological expansion has become one of the greatest challenges in modern day physics [see e.g., [1]]. Of the many potential explanations, two classes are popular today: ones that propose a new and unseen form of energy with negative pressure, and ones that modify the Einstein-Hilbert action. Of particular interest in recent literature are a class of modifications to the Einstein action by an addition of nonlinear functions of the Ricci scalar, $R$, which have been demonstrated to cause accelerated expansion for a range of $f(R)$ functions [2–4]

In addition to explaining the cosmic acceleration, such $f(R)$ modifications must satisfy stringent constraints imposed by solar-system tests [5–8] as well as cosmological constraints imposed by recent dark energy measurements [9–11]. Recently, a new class of $f(R)$ models were proposed by Hu and Sawicki [[12], hereafter HS model] that has the flexibility to reproduce the observed cosmological acceleration as well as to satisfy solar-system bounds on deviations from the Newtonian limits of general relativity. In the proposed model, the scalar degree of freedom introduced by the $f(R)$ modification becomes massive in regions of high curvature and is hidden by the so-called chameleon mechanism [13,14].

In such models that evade both the cosmological background test and solar-system tests, the next strongest constraint comes from the effects of the $f(R)$ modifications to the intermediate lengths scales, in the regime of cosmological large scale structures. Outside of dense dark matter halos, the light scalar degree of freedom produces a long range fifth force that enhances gravitational attraction and thereby potentially changes clustering of matter. Such effects were studied in the linear regime [12,15,16], in which large deviations of the dark matter power spectrum were obtained even for small $f(R)$ modifications. Furthermore, an attempt to model some of the nonlinear chameleon physics using a parametrized framework on top of a halo model are presented in [17]. However, those studies remain inconclusive because the effects of nonlinear growth of structure and the chameleon mechanism (which requires nonlinear growth) are not included in the analyses. For such a nonlinear study, a realistic $N$-body simulation of structure formation in $f(R)$ cosmologies is needed.

In this paper, we introduce a formalism and an implementation of a cosmological $N$-body simulation with fully nonlinear treatment of $f(R)$ modifications. Although somewhat limited in the attainable dynamic range, we show that our implementation can capture the essential nonlinear features of the HS model that have large impact on the cosmological large scale structure formation. In a companion paper, we apply our methodology to realistic cosmological simulations and discuss the implications of the $f(R)$ model on the large scale structure of the Universe.

This paper is organized as follows. In Sec. II, we review the general properties of $f(R)$ cosmology and give details on the particular model of $f(R)$ that we choose. The numerical algorithms to solve for the $f(R)$ cosmological large scale structure formation are developed in Sec. III, and are tested in Sec. IV. Several test cases under the HS model, highlighting the different aspects of the $f(R)$ model, are presented in Sec. V. In addition, a brief discussion of full cosmological simulations with $f(R)$ mod-

*oyachai@uchicago.edu

 

ifications are presented in Sec. V; a more complete discussion will be presented in a companion paper. Finally, conclusions and discussions of the possible future extension of our formalism are given in Sec. VI.

## II. $f(R)$ COSMOLOGY

The so-called $f(R)$ theories are modifications to general relativity (GR) given by the following action:

$$S = \int d^4x\sqrt{-g}\left\{\frac{R + f(R)}{2\kappa^2} + L_m\right\}, \tag{1}$$

where $R$ is the scalar curvature (i.e., the Ricci scalar), $f(R)$ is an arbitrary function of $R$, $\kappa^2 = 8\pi G$, and $L_m$ is the Lagrangian of the ordinary matter. Setting $f(R) = 0$ recovers ordinary GR without a cosmological constant, while $f(R) = f_c$, where $f_c$ is a constant, is equivalent to GR with a cosmological constant. We follow the standard procedure of setting $c = 1$ and $\hbar = 1$ throughout the paper unless otherwise noted. The variation of the action with respect to the metric results in the field equation for $g_{\alpha\beta}$,

$$G_{\alpha\beta} + f_R R_{\alpha\beta} - \left(\frac{f}{2} - \Box f_R\right)g_{\alpha\beta} - \nabla_\alpha\nabla_\beta f_R = \kappa^2 T_{\alpha\beta}, \tag{2}$$

where $f_R \equiv \frac{df(R)}{dR}$, $G_{\alpha\beta}$ is the unmodified Einstein tensor, and $T_{\alpha\beta}$ is the energy-momentum tensor. We work with the standard assumption that the Universe is filled with a perfect fluid of the form

$$T_{\alpha\beta} = (\rho + P)U_\alpha U_\beta + P g_{\alpha\beta}, \tag{3}$$

where $\rho$ and $P$ are the fluid energy density and pressure and $U$ is the four velocity of the fluid. Because we are only concerned with modeling the effects of late time accelerated expansion, we neglect the relativistic energy component and thus set $P = 0$. For the background Friedmann-Robertson-Walker (FRW) metric, the modified Einstein equation becomes the modified Friedmann equation

$$H^2 - \bar{f}_R(HH' + H^2) + \frac{\bar{f}}{6} + H^2\bar{f}_{RR}\bar{R}' = \frac{\kappa\bar{\rho}}{3}, \tag{4}$$

where $H$ is the Hubble parameter, $\bar{f}_{RR}$ is the second derivative of $\bar{f}$ with respect to $R$, and $'$ denotes derivatives with respect to $\ln a$. The overbars signify that the quantities are defined at the cosmological background level. The trace of Eq. (2) becomes a dynamical equation for a scalar field $f_R$ that couples to the metric:

$$3\Box f_R - R + f_R R - 2f = -\kappa^2\rho. \tag{5}$$

We note that this equivalence to a scalar-tensor theory of gravity can be made exact through a conformal transformation to the Einstein frame (see e.g. [18]). We choose to work in the original Jordan frame so that the equations of motion for the matter given the metric remain exactly the same as usual.

Recently, a phenomenologically viable model of $f(R)$ was proposed in [12,17], in which

$$f(R) = -m^2\frac{c_1(R/m^2)^n}{c_2(R/m^2)^n + 1}, \tag{6}$$

where $c_1$, $c_2$, and $n$ are free positive dimensionless parameters and

$$m^2 \equiv \frac{8\pi G\bar{\rho}_M}{3}. \tag{7}$$

This form of $f(R)$ can be tuned to match the $\Lambda$CDM expansion history while not introducing a true cosmological constant. In addition, the above form has the potential to evade solar-system tests via the so-called chameleon mechanism [13,14] in which the scalar field responsible for the modified gravity ($f_R$) is suppressed in regions of high density and curvature, thus remaining viable even with the stringent constraints placed by such tests. However, the HS model has interesting deviations from $\Lambda$CDM in the intermediate scales that result in distinct signatures in large scale structure formation. Such deviations have been studied in the linear regime [15,16,19], but the lack of insights into the modification's behavior in the nonlinear regime places a strong limitation on the applicability of comparison of such studies to observations. In particular, the chameleon mechanism is a manifestation of the nonlinear coupling between the scalar field and the metric perturbations and thus will not be captured in linear studies. We defer the discussions of physical interpretations and consequences of the chameleon mechanism to the companion paper.

The free parameters $c_1$, $c_2$, and $n$ are chosen so that the resulting background expansion history closely matches that of $\Lambda$CDM. This requirement is equivalent to requiring the background $f_R$ field strength today, $\bar{f}_{R0}$, to be sufficiently small ($\bar{f}_{R0} \ll 1$) or, alternatively, $R_0 \gg m^2$. In this parameter regime, the field is always near the minimum of the effective potential,

$$\frac{\partial V_{\rm eff}}{\partial f_R} \equiv \frac{1}{3}(R - f_R R + 2f - \kappa^2\rho), \tag{8}$$

and thus we have

$$\bar{R} \approx 8\pi G\bar{\rho}_{\rm M} - 2\bar{f} \approx 8\pi G\bar{\rho}_{\rm M} + 2\frac{c_1}{c_2}m^2. \tag{9}$$

In the limit of $\Lambda$CDM, we have

$$\bar{R}_{\Lambda\rm CDM} = 3m^2\left(a^{-3} + 4\frac{\Omega_\Lambda}{\Omega_{\rm M}}\right), \tag{10}$$

and thus, to approximate the $\Lambda$CDM expansion history, we set

$$\frac{c_1}{c_2} = 6\frac{\Omega_\Lambda}{\Omega_{\rm M}}. \tag{11}$$

Note that today, with $\Omega_{\rm M,0} \approx 0.24$ and $\Omega_{\Lambda,0} \approx 0.76$, we have $R_0 \approx 41m^2 \gg m^2$. Two free parameters remain, namely $n$ and $c_1/c_2^2$, that control how closely the $f(R)$ expansion history matches that of $\Lambda$CDM. From the high curvature limit of $f(R)$,

$$\bar{f}(\bar{R} \gg m^2) \approx -\frac{c_1}{c_2}m^2 + \frac{c_1}{c_2^2}m^2\left(\frac{m^2}{\bar{R}}\right)^n, \tag{12}$$

we see that larger $c_1/c_2^2$ results in closer match to $\Lambda$CDM (i.e., $\bar{f}(\bar{R})$ approaches a constant as $c_1/c_2^2 \to 0$) and smaller $n$ mimics $\Lambda$CDM until later in the expansion history. It is also important to note that the condition $\bar{R}_0 \gg m^2$ requires that $\bar{R} \gg m^2$ at the background level throughout the expansion history because $\bar{R}$ is a monotonically decreasing function of time. Thus, in our numerical simulations, we are able to simplify the field equations given the high curvature assumption.

Phenomenologically viable $f(R)$ models require that $|f_{R0}|$ be small so as to not significantly alter the cosmic expansion history, limiting the field strength to $|f_{R0}| \sim 1$ with current observations [19] and to $|f_{R0}| \sim 0.01$ with future weak lensing surveys [12]. An even stronger constraint can be placed on the field by considering the dynamics of our galaxy, resulting in an upper bound of $|f_{R0}| \sim 10^{-6}$ [12]. However, such analyses do not self-consistently model large scale clustering that potentially relaxes the tight upper bound.

In the high curvature regime, our $f(R)$ model can be expanded as

$$f_R = -\frac{nc_1(R/m^2)^{n-1}}{(c_2(R/m^2)^n + 1)^2} \approx -\frac{nc_1}{c_2^2}\left(\frac{m^2}{R}\right)^{n+1}, \tag{13}$$

valid when $R \gg m^2$. Furthermore, the field equation (5) can be simplified by neglecting the small $f_R R$ term, thus resulting in

$$3\Box f_R - R - 2f = -\kappa^2\rho. \tag{14}$$

Assuming the FRW metric, we subtract the spatially constant background quantities and thus the field equation becomes an equation for the perturbations,

$$3\Box\delta f_R - \delta R = -\kappa^2\delta\rho, \tag{15}$$

where $\delta R \equiv R - \bar{R} \equiv R - R_{\Lambda\mathrm{CDM}}$, $\delta f_R = f_R - f_R(\bar{R})$, $\delta\rho = \rho - \bar{\rho}$, and the term proportional to $\delta f \approx f_R\delta R$ has been neglected because $f_R \ll 1$. Finally, we work in the quasistatic limit in which $\nabla f_R \gg \partial f_R/\partial t$, and the field equation is reduced to

$$\nabla^2 f_R = \tfrac{1}{3}[\delta R(f_R) - 8\pi G\delta\rho]. \tag{16}$$

Because $f(R)$ is a metric theory of gravity, dark matter particles move along the geodesics of the metric, just as in ordinary gravity. The $f_R$ field is coupled to the gravitational potential, $\phi$, via

$$\nabla^2\phi = \frac{16\pi G}{3}\delta\rho - \frac{1}{6}\delta R(f_R), \tag{17}$$

which can be derived by evaluating the time-time component of Eq. (2) in the large curvature limit [see [12] for more details]. Equations (16) and (17) define a system of equations for the gravitational potential, the solution to which can be used to evolve matter particles. Note that in the limit of ordinary GR, $\delta R = 8\pi G\delta\rho$, and the equation for the gravitational potential reduces to the unmodified equation,

$$\nabla^2\phi = 4\pi G\delta\rho. \tag{18}$$

The strategy that we use to simulate $f(R)$ cosmology boils down to solving the two field equations, Eq. (16) and (17), and using the resulting peculiar potential to update the dark matter density.

## III. NUMERICAL METHODS

Our $N$-body simulation is based on the particle-mesh algorithm (hereafter PM), in which the particle densities are interpolated onto a regular grid and the potential is solved only at the grid points [see, e.g., [20,21]]. The choice to use a field representation of the potential instead of particle pair representation (as in Tree codes) is motivated by the fact that the change in the interparticle forces are mediated by an auxiliary scalar field, namely $f_R$. The force law between a pair of particles in the presence of $f_R$ depends on the entire behavior of the field between the two particles and thus cannot be expressed as a simple function of their separation. In this section, we outline the method we developed to obtain $\phi$ by numerically solving Eqs. (16) and (17).

### A. Code units

The code units are based on the convention used in [22,23], where

$$\tilde{r} = a^{-1}\frac{r}{r_0}, \qquad \tilde{t} = \frac{t}{t_0}, \qquad \tilde{p} = a\frac{v}{v_0},$$
$$\tilde{\phi} = \frac{\phi}{\phi_0}, \qquad \tilde{\rho} = a^3\frac{\rho}{\rho_0}, \qquad \tilde{R} = a^3\frac{R}{R_0},$$

and

$$r_0 = \frac{L_{\mathrm{box}}}{N_g}, \tag{19}$$

$$t_0 = H_0^{-1}, \tag{20}$$

$$v_0 = \frac{r_0}{t_0}, \tag{21}$$

$$\rho_0 = \rho_{c,0}\Omega_{\mathrm{M},0}, \tag{22}$$

$$\phi_0 = v_0^2, \tag{23}$$

$$R_0 = m_0^2 = \frac{8\pi G\rho_0}{3}. \quad (24)$$

In the above definitions, $L_{\rm box}$ is the comoving simulation box size in $h^{-1}$ Mpc, $N_g$ is the number of grid cells in each direction, $H_0$ is the Hubble parameter today, $\rho_{c,0}$ is the critical density today, and $\Omega_{\rm M,0}$ is the fraction of non-relativistic matter today relative to the critical density.

Before converting the field equations to code units, we restore the factors of $c$ in Eq. (16), which results in

$$\nabla^2 f_R = \frac{1}{3c^2}[\delta R(f_R) - 8\pi G\delta\rho]. \quad (25)$$

Substituting all physical quantities and derivatives in Eq. (25) by their code unit equivalent yields

$$\tilde{\nabla}^2\delta f_R = \frac{\Omega_{\rm M,0}}{a\tilde{c}^2}\left[\frac{\delta\tilde{R}}{3} - \delta\right], \quad (26)$$

where

$$\delta = \frac{\rho - \bar{\rho}}{\bar{\rho}}. \quad (27)$$

The quantity $\tilde{c}$ is the speed of light in code units, i.e., $\tilde{c} = c/v_0$. Similarly, we transform Eq. (17) into code units and obtain

$$\tilde{\nabla}^2\tilde{\phi} = \frac{\Omega_{\rm M,0}}{a}\left[2\delta - \frac{1}{6}\delta\tilde{R}\right]. \quad (28)$$

From this point on, we work in code units unless otherwise specified, and we drop the tilde from code variables.

### B. Solving for $f_R$ and $\phi$

The field equation for $f_R$ is a nonlinear elliptical partial differential equation because the function $R(f_R)$ is nonlinear in general. Because of this nonlinearity, standard spectral methods [e.g., fast Fourier transform (FFT) method] are not applicable and we therefore resort to a nonlinear relaxation method for the solution. Given a general partial differential equation,

$$L(u) = f, \quad (29)$$

where $L(u)$ is a nonlinear differential operator on the field $u$ and $f$ is the source term, let us define

$$\mathcal{L}(u) \equiv L(u) - f. \quad (30)$$

The problem of finding the solution, $u$, for Eq. (29) becomes a problem of finding the root of $\mathcal{L}(u)$. The root finding is carried out by an iterative Newton-Raphson algorithm, which defines the relaxation method [see, e.g., [24]],

$$u^{\rm new} = u^{\rm old} - \frac{\mathcal{L}(u^{\rm old})}{\partial\mathcal{L}/\partial u^{\rm old}}. \quad (31)$$

The only remaining difficulty is determining the appropriate form of $\mathcal{L}(u)$ and its discretization. For our model of $f(R)$, the differential operator $\mathcal{L}(f_R)$ is defined as

$$\mathcal{L}(f_R) = \frac{ac^2}{\Omega_{\rm M,0}}\nabla^2 f_R - \frac{R(f_R) - \bar{R}}{3} + \delta. \quad (32)$$

A naive and straightforward discretization of Eq. (26) suffers from severe numerical instability. The differential operator in Eq. (32) is not defined for non-negative values of $f_R$ [see Eq. (13)], and thus the iterative solution fails as soon as an iteration oversteps the true solution into the forbidden region. We find that placing an artificial ceiling on the value of $f_R$ does not adequately solve the problem because the stability becomes conditional on very precise tuning of the ceiling due to the steepness of $R(f_R)$ near $f_R = 0$. The best way to avoid the problem in this model is to redefine the field as

$$f_R = \bar{f}_R e^u \quad (33)$$

and solve for $u$ instead of $f_R$. With this substitution, the new field $u$ has infinite domain and does not suffer from abrupt instabilities. The differential operator thus becomes

$$\mathcal{L}(f_R) = \frac{ac^2}{\Omega_{M,0}}\bar{f}_R\nabla\cdot(e^u\nabla u) - \frac{R(\bar{f}_R e^u) - \bar{R}}{3} + \delta. \quad (34)$$

In our implementation, the differential operator is discretized as a variable coefficient Poisson equation, in which the value of $u$ at a grid cell identified by $i$, $j$, and $k$ is updated using the red-black Newton-Gauss-Seidel (NGS) scheme [24]. The actual discretization is too long to be displayed in the body of the text, and is instead placed in Appendix A. We use periodic boundary conditions to close the NGS scheme at the edges of our simulation boxes.

One potential problem with this substitution is the fact that we added additional nonlinearity into a problem that is already highly nonlinear. In particular, the additional nonlinearity is exponential, and thus the errors in the discretized solution, $u_{i,j,k}$, are potentially enhanced exponentially. In our experience running cosmological simulations with $f(R)$ modification, we find that the effects of this addition are negligible in all cases and the iterations converge to the same solution whether this substitution is made or not, while avoiding the singularity of the curvature field at $f_R = 0$.

Given the solution to $f_R$ using the NGS algorithm and the density field, we can compute the solution to $\phi$ using Eq. (28). The equation is a standard linear Poisson equation and thus is solved efficiently using the fast Fourier transform method. We adopt the cloud-in-cell density interpolation algorithm (hereafter CIC), which treats a particle as a uniform density cube that is equal in size to the underlying grid cell, to compute the density field.

### C. Multigrid acceleration

In general, relaxation methods for solutions of partial differential equations are very inefficient and computationally expensive. However, this inefficiency can be mostly alleviated by the use of multigrid techniques. The multigrid method [25] is a class of algorithms to solve partial differential equations using a hierarchy of discretizations with increasingly coarse grids. In particular, it exploits the fact that typical relaxation schemes, such as the NGS scheme previously detailed, smooth out the high frequency residual errors faster than the low frequency error modes. Thus, by interpolating the low frequency error modes onto a coarser grid, the same error mode now appears as a high frequency mode on the coarser grid and can be efficiently reduced by relaxation passes on that grid.

In our working code, we implement a particular type of multigrid method called the full approximation scheme ([26], hereafter FAS), which is particularly suited for nonlinear boundary value partial differential equations. In order to define the FAS algorithm, we first define two grids, the fine grid ($\Omega_h$) and the coarse grid ($\Omega_{2h}$). In addition, we define two intergrid operators, one that restricts a fine grid field onto a coarse grid and one that interpolates a coarse grid field onto a fine grid. We label the former as $I_h^{2h}$ and the latter as $I_{2h}^h$, and we leave the details of their implementations to Appendix B. Finally, we denote the quantities defined on a coarse grid by a superscript $2h$ and the quantities defined on a fine grid by a superscript $h$.

The two grid FAS scheme can be summarized by the following. Given the initial guess to the solution, $u^h$, the FAS algorithm can be summarized as follows:

(i) Relax on $\Omega_h$ (presmoothing)
(ii) Compute: $f^{2h} = I_h^{2h}(f^h - L^h(u^h)) + L^{2h}(I_h^{2h}u^h)$
(iii) Solve: $L^{2h}(u^{2h}) = f^{2h}$
(iv) Correct the solution: $u^h_{\rm new} = u^h + I_{2h}^h(u^{2h} - I_h^{2h}u^h)$
(v) Relax on $\Omega_h$ (post-smoothing)

In a true multigrid method, the third step above is also carried out using a multigrid method, thus forming the recursive hierarchy of coarser grids. The recursion is stopped when the number of coarse grid cells per dimension reaches four; the solution at this level is obtained by iterating NSG until convergence. All relaxations are carried out using the NGS scheme that is appropriate for the given coarse (or fine) grid.

In our implementation, we use the full-weighted restriction operator ($I_h^{2h}$) and its adjoint, the bilinear interpolation as the prolongation operator ($I_{2h}^h$). In practice, we find that the choice of the restriction and prolongation operators does not affect the stability of convergence for most typical cosmological simulations. However, we find the convergence rate when using full-weighting and bilinear interpolation to be better than other, simpler choices.

### D. Particle dynamics

Given the solution for the $f_R$ field, the Newtonian potential is computed by solving Eq. (28), which is a linear Poisson equation with a nonstandard (i.e., non-GR) source term. Because of its linearity, such an equation can be solved efficiently using a fast Fourier transform method (see [20]). The forces on the dark matter particles are computed using Newton's equations in comoving code coordinates,

$$\frac{dx}{da} = \frac{p}{\dot{a}a^2}, \tag{35}$$

$$\frac{dp}{da} = -\frac{\nabla\phi}{\dot{a}}. \tag{36}$$

Because the expansion history of our $f(R)$ model is tuned to that of flat $\Lambda$CDM, $\dot{a}$ is computed simply as

$$\dot{a} = a^{-1/2}\sqrt{\Omega_{\rm M,0} + \Omega_{\Lambda,0}a^3}, \tag{37}$$

where the overdot denotes a derivative with respect to coordinate time in code units. The gradient of the gravitational potential is computed using a standard finite difference scheme consistent with our grid density assignment operator, namely, the CIC scheme. We evolve the particles using a second-order accurate leap-frog method [27].

## IV. TESTS OF THE CODE

Our $N$-body simulation is implemented in C++ with shared memory parallelization using OPENMP. In the following subsections, we present various tests of the implementation to assess the correctness of the code as well as its computational speed.

### A. Analytically tractable case

First, we construct a density field $\delta$ that has a known $f_R$ solution to check that the code can recover the true solution. In 1D, the field equation (26) becomes

$$\frac{\partial^2 f_R}{\partial^2 x} = \frac{\Omega_{\rm M,0}}{ac^2}\left(\frac{\delta R}{3} - \delta\right), \tag{38}$$

which, after setting all constants to 1 and taking $n = 1$ and $\bar{R} = 1$, is

$$\frac{\partial^2 f_R}{\partial^2 x} = \frac{1}{3}[(-f_R)^{-1/2} - 1 - 3\delta]. \tag{39}$$

We take the analytic solution to be

$$f_R = \sin\left(\frac{2\pi x}{L_{\rm box}}\right) - 2, \tag{40}$$

and substitute the solution into Eq. (39) to find

$$\delta = \left(\frac{2\pi}{L_{\rm box}}\right)^2 \sin\left(\frac{2\pi x}{L_{\rm box}}\right) + \frac{1}{3}\left[2 - \sin\left(\frac{2\pi x}{L_{\rm box}}\right)\right]^{-1/2} - \frac{1}{3}. \tag{41}$$

Thus, setting the density field to the expression in (41) and numerically solving for $f_R$ allows us to compare the code accuracy against the known solution, Eq. (40).

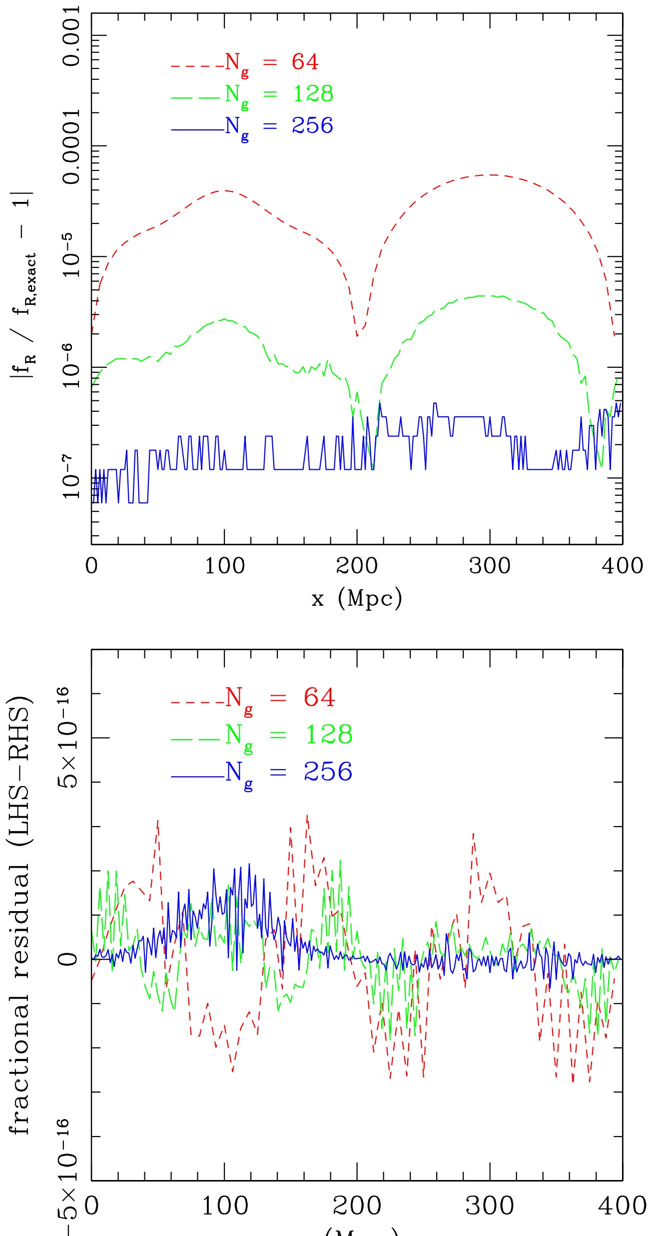


FIG. 1 (color online). The fractional discretization error (left), shown as $|f_{R,\mathrm{code}}/f_{R,\mathrm{exact}} - 1|$, and the fractional residual error (right), $\mathcal{L}(f_R)$, for the analytically tractable case of Sec. IV A. The discretization error for the highest resolution box is $\sim 10^{-6}$, and it allows us to define a sensible stopping criteria for the multigrid iterations. The fractional residual error is floored by limits on machine accuracy, which is $\sim 10^{-15}$.

In Fig. 1, we show the results of applying our code to this problem with three different grid resolutions. In the left panel, fractional discretization errors, defined as $f_{R,\mathrm{code}}/f_{R,\mathrm{exact}} - 1$, are shown, and the residual errors, defined as $\mathcal{L}(u)$, are shown in the right panel. The average discretization error decreases by approximately an order of magnitude for each twofold increase in grid resolution. Thus, for $N_g = 512$, we expect the discretization error to be on the order of $10^{-7}$, and therefore it gives us a useful stopping criteria for solution convergence based on the requirement that the discretization error is the dominant source of error. We terminate the iterative multigrid process when the residual error (which can be computed without knowing the true solution) is smaller than $10^{-10}$, guaranteeing the residual error to be much smaller than the discretization error for our highest resolution simulations.

### B. Point mass

In this test, we place a point mass (consistent with the CIC scheme) at the origin of a periodic simulation box, with the corresponding density field given by

$$\delta^{(1)}_{i,j,k} = \begin{cases} 10^{-4}N_g^3 & \text{if } i = j = k = 0 \\ -10^{-4} & \text{otherwise} \end{cases}, \tag{42}$$

where the indices $i$, $j$, and $k$, refer to the grid cell indices in $x$, $y$, and $z$ directions, respectively. In the subsequent discussion in this section, we restore the tilde notation to distinguish code variables and physical variables. With this density configuration, outside the grid cell at the origin, we expect that

$$\tilde{\nabla}^2 \delta f_R \approx \frac{\Omega_{\mathrm{M},0}}{a\tilde{c}^2}\delta\tilde{R} \approx 3\frac{\Omega_{\mathrm{M},0}}{a\tilde{c}^2} m_{\mathrm{eff}}^2 \delta f_R, \tag{43}$$

where $m_{\mathrm{eff}}$ is the effective field mass of the $f_R$ field, given in physical coordinates by

$$m_{\mathrm{eff}}^2 = \frac{1}{3}\left(\frac{1+f_R}{f_{RR}} - R\right) \approx \frac{1}{3} f_{RR}^{-1} \tag{44}$$

for small $f_R$. The quantity $f_{RR}$ is the second derivative of $f(R)$ with respect to $R$. Thus, the solution to Eq. (43) is a Yukawa-like potential,

$$\delta f_R \propto \frac{e^{-\tilde{m}_{\mathrm{eff}} r}}{r}, \tag{45}$$

where

$$\tilde{m}_{\mathrm{eff}} = \sqrt{3\frac{\Omega_{\mathrm{M},0}}{a\tilde{c}^2}} m_{\mathrm{eff}} \tag{46}$$

is the effective comoving field mass in code units.

Figure 2 shows the $f_R$ field solution computed on a $N_g = 256$ grid. The simulation parameters were: $L_{\mathrm{box}} = 400$ Mpc, $\Omega_{\mathrm{M},0} = 0.3$, $\Omega_{\Lambda,0} = 0.7$, $h = 0.7$, and $f_{R,0} = -10^{-5}$. On the same plot, the analytic solution with the expected $\tilde{m}_{\mathrm{eff}}$ is plotted. The $\sim 10\%$ discrepancy at $x \sim 2h^{-1}$ Mpc is due to the fact that the approximation $\delta R \approx m_{\mathrm{eff}}^2 \delta f_R$ is only valid for small $\delta f_R$ and thus is only appropriate at large distances away from the central near point mass. Hence, the Yukawa solution in Fig. 2 is normalized such that the solution best matches the simulation at $x \sim 10h^{-1}$ Mpc where the $\delta f_R$ becomes sufficiently small. At $x \gtrsim 40h^{-1}$ Mpc, the solution $\delta f_R$ approaches

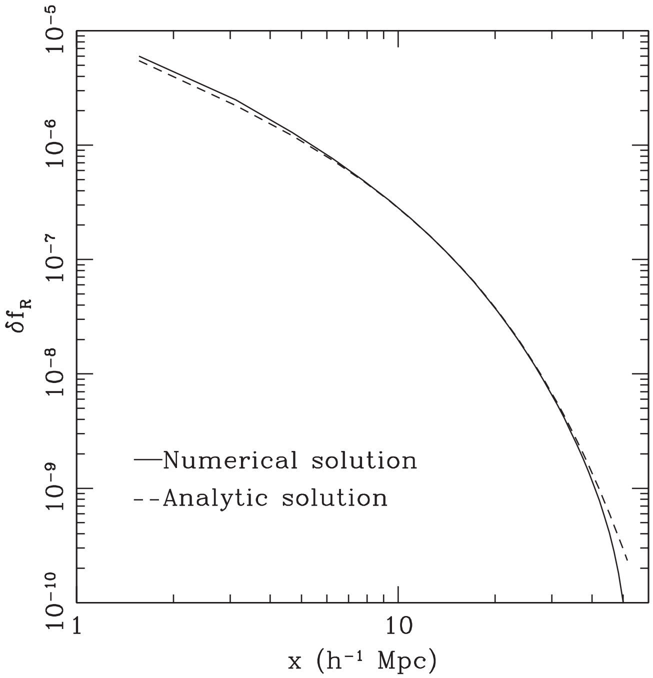


FIG. 2. The computed and expected solutions for the point mass test. The analytic solution is arbitrarily normalized such that it and the numerical solutions match at scales where the simulation is expected to best match the analytic solution. This scale corresponds to $x = 10h^{-1}$ Mpc. The background effective field mass is $0.13h$ $\mathrm{Mpc}^{-1}$.

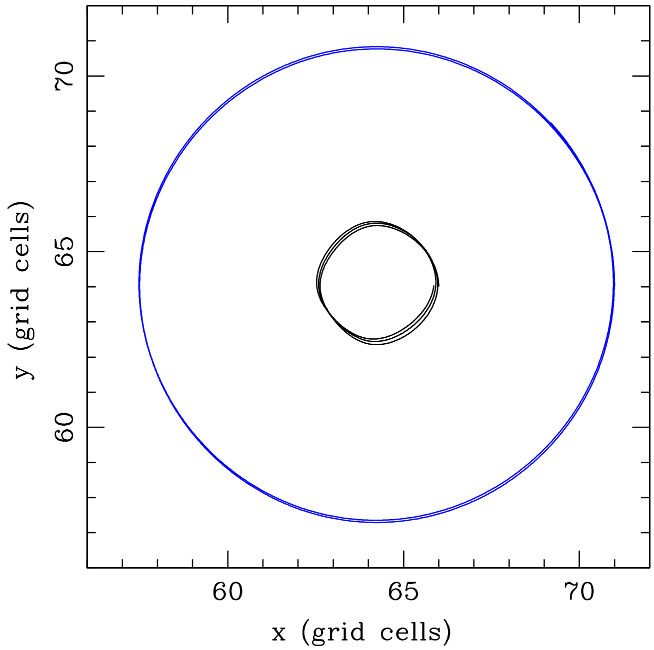


FIG. 3 (color online). Orbit test. A point mass is placed at the center of a $128^3$ grid, and the trajectory of test particles are simulated without $f(R)$ modification. The inner particle is placed at two grid cells away from the center, while the outer particle is placed seven grid cells away. Both particles are given initial velocities such that they would be in circular orbit without $f(R)$ modifications.

the level of discretization error for $N_g = 256$ ($\sim 10^{-6}$) and hence begins to show deviations from the analytic solution.

### C. Dynamics

As previously described in Sec. III D, the particle trajectories are integrated using a second-order accurate leapfrog scheme. In Fig. 3, we show the orbits of test particles orbiting around a central point mass. The test particles are placed at two and seven grid cells away from the point mass and are given initial velocity such that they would be in circular orbits if there were no integration errors and no $f(R)$ modifications. The solid lines show the simulated orbit for the two different radii. Far away from the point source, where the forces are adequately resolved, the orbit is nearly circular as expected for unmodified GR. The smaller orbit, with a theoretical radius of two grid cells, is not well resolved by the underlying potential grid. However, the simulated orbit is still nearly circular, with only a few percent deviation after two complete orbits. The two-body force law, and its modifications due to $f(R)$ models, will be further studied in Sec. V A.

Another popular test of the particles dynamics as well as of the accuracy of the potential solver is the Zeldovich pancake collapse test [23,28,29]. The evolution of a 1D sine wave is described exactly by the Zeldovich solution,

$$x_i(a) = q_i + AG(a)\sin\left(\frac{2\pi q_i}{L_{\mathrm{box}}}\right), \tag{47}$$

$$p_i(a) = Aa^2\dot{G}(a - \Delta a/2)\sin\left(\frac{2\pi q_i}{L_{\mathrm{box}}}\right), \tag{48}$$

where $q_i = i\Delta x$, $G(a)$ is the linear growth function, $\Delta a$ is the time step used in the simulation, and $A$ is a normalization constant that fixes the time at shell crossing. By setting the initial conditions at $a = a_{\mathrm{init}}$ according to the Zeldovich solution, we can compare the subsequent particle evolution to the same solution to gauge the accuracy of our particle dynamics.

For our test, we use $\Omega_{\mathrm{M},0} = 0.24$, $\Omega_{\Lambda,0} = 0.76$, $h = 0.73$, and no $f(R)$ modifications. The simulation box is set to $L_{\mathrm{box}} = 100h^{-1}$ Mpc, and we use $64^3$ particles and $64^3$ grid cells. Figure 4 shows the particle momenta versus the particle positions at the time of shell crossing, which is set to be $a = 1$. The dots denote the simulation output and the line represents the exact solution given by the Zeldovich approximation. As expected, the agreement between our code and the Zeldovich solution is good, with maximum deviation less than 1%.

As another check of the particle dynamics, we have run several cosmological simulations without $f(R)$ modifications to check our results against the Smith *et al.* fits to the power spectrum [30]. We run three simulations with box

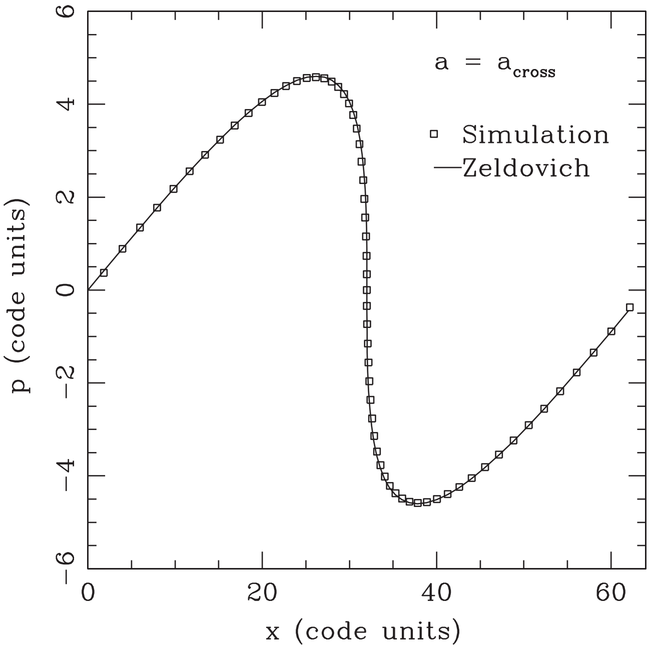


FIG. 4. Zeldovich 1D plane wave collapse with no $f(R)$ modifications. Particle momenta ($p$) is plotted against particle positions ($x$). The points represent the simulation output and the line represents the exact solution given by the Zeldovich approximation. The snapshot is taken at $a = a_{\rm cross} = 1$.

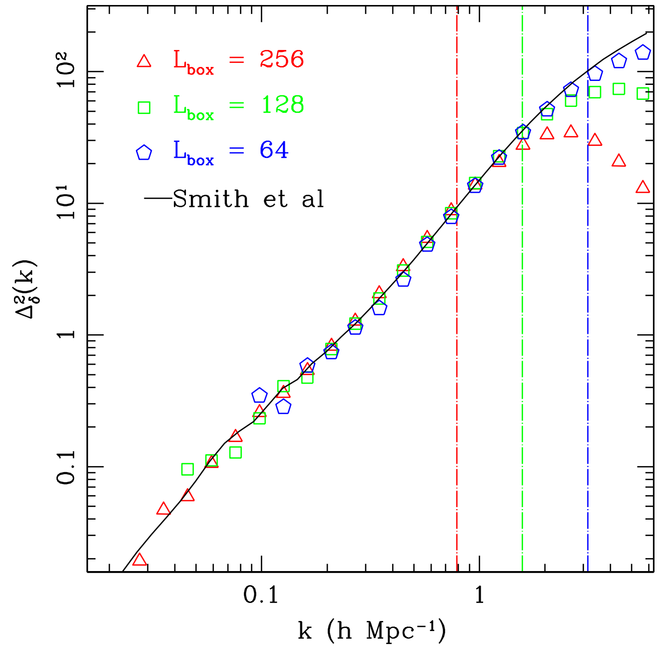


FIG. 5 (color online). Power spectra computed from cosmological simulations without $f(R)$ modifications. The Smith *et al.* fit is plotted in a solid line, showing good agreement with our simulations. The vertical lines, from left to right, are the particle half-Nyquist scales, defined as $k_{\rm hN} = \pi N_p/(4L_{\rm box})$, for $L_{\rm box} =$ 256, 128, and $64h^{-1}$ Mpc boxes.

sizes ($L_{\rm box}$) of $256h^{-1}$ Mpc (L256), $128h^{-1}$ Mpc (L128), and $64h^{-1}$ Mpc (L64). All simulations have the following cosmological parameters resembling the third year Wilkinson Microwave Anisotropy Probe [[11], WMAP3] results: $\Omega_{\rm M,0} = 0.24$, $\Omega_{\Lambda,0} = 0.76$, $\Omega_{\rm b,0} = 0.041\,81$, $H_0 = 72$ km/s/Mpc, and $\sigma_8 = 0.8$. We take the slope of the primordial power spectrum, $n$, to be 0.958.

The initial conditions for the simulations are created using ENZO [31], a publicly available cosmological $N$-body + hydrodynamics code. ENZO uses the Zeldovich approximation to displace particles on a uniform grid according to a given initial power spectrum. We use the initial power spectra given by Eistenstein and Hu [32], not including the effects of baryon acoustic oscillations. The simulations are started at $z = 49$.

All simulations are run with 512 grid cells in each direction (i.e., $N_g = 512$) and with $256^3$ particles. Thus, the formal spatial resolutions of the simulations are $0.5h^{-1}$ Mpc, $0.25h^{-1}$ Mpc, and $0.125h^{-1}$ Mpc for the largest, middle, and smallest boxes, respectively. The corresponding mass resolutions are $2.76 \times 10^{11} {\rm M}_\odot$, $3.45 \times 10^{10} {\rm M}_\odot$, and $4.31 \times 10^9 {\rm M}_\odot$.

For each simulation box configuration, we run multiple simulations with different realization of the initial power spectrum in order to reduce a finite sample variance. Two L256 simulations, three L128 simulations, and four L64 simulations were run.

In Fig. 5, we show the power spectrum of our simulations as well as the Smith *et al.* fit. Multiple simulations of the same box size are averaged in the figure. The vertical lines denote the half-Nyquist scale of the particles, plotted as a rough guide to show the resolution limits of our simulations. We see from the plot that our simulations match the Smith *et al.* fit to within ~10% at most scales smaller than the half-Nyquist scale. The large scatter at low $k$ is seen because only a small number of the largest wavelength modes can fit in a simulation box.

### D. Time derivative

In our simulation, we work in the quasistatic limit of the full field equation for $f_R$, Eq. (5), in which we neglect the time derivative term. There is no simple way to check the validity of our assumption short of running a full simulation including the time derivative term; nevertheless, we can check that our assumption is at least self-consistent by running modified cosmological simulations with quasistatic assumption and comparing the time derivative of the $f_R$ field to its spatial derivative.

We use the same simulation setup as the cosmological simulations in Sec. IV C except for the inclusion of $f(R)$ modification with $f_{R0} = -10^{-5}$. The time derivative of the field is estimated by the finite differencing of fields at successive time steps. In Fig. 6, we show the fraction of the 2-norms of the time derivative and spatial derivatives of the field at different scale factors. Although the ratio varies by time, we see that the time derivative is generally much

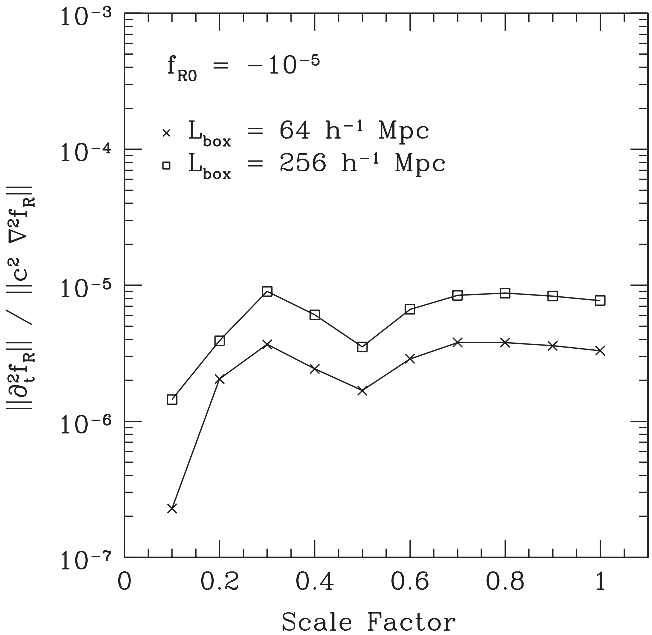


FIG. 6. The ratio of the time derivative of the $f_R$ field to the spatial gradient. The 2-norm is defined simply as $\sqrt{\langle x^2 \rangle}$, where $x$ is either $\partial_t^2 f_R$ or $\nabla^2 f_R$. The factor of $c^2$ comes from the definition of the FRW metric.

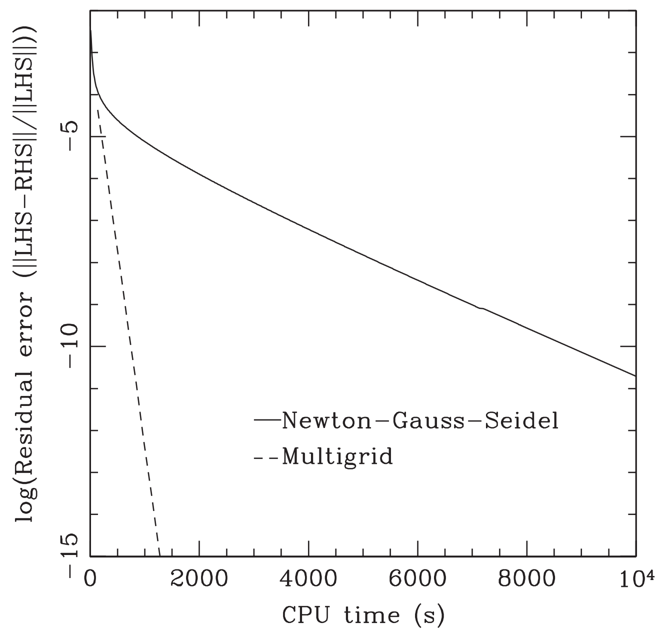


FIG. 7. The residual error, defined as the 2-norm of the left-hand side minus the right-hand side of Eq. (43) divided by the 2-norm of the left-hand side, is plotted as a function of CPU time spent in the iterative partial differential equations (PDE) solvers. The NGS scheme is only efficient at reducing low wavelength error modes and thus the convergence rate stalls as the large wavelength mode begins to dominate the error budget. The multigrid scheme can reduce error modes of all sizes equally well, and thus retains a good convergence rate throughout the iterations.

smaller than the spatial derivative and thus that our simulations are consistent with our assumptions.

### E. Code timing and memory requirement

Even with the efficiency of the multigrid method, solving a 3D nonlinear partial differential equation with reasonable resolution is still a computationally expensive endeavor. In Fig. 7, we plot the residual error as a function of the CPU time spent during the NGS and multigrid iterations of the point mass solution studied in Sec. IV B. The computations were carried out on a 2.8 GHz AMD Opteron 2220 processor without using OPENMP multithreading (i.e., single threaded). For the NGS method, the high frequency error modes are reduced more efficiently than low frequency modes. Thus, the residual error goes down fast during the initial few hundred seconds of the NGS iterations, until the low frequency error modes dominate the overall residual error budget. Thereafter, the iterations converge slowly, rendering the method unacceptable for cosmological simulations in which the $f_R$ field must be evaluated hundreds of times. With the multigrid method, because of its use of coarse grids, error modes of all frequencies decay at nearly the same rate, and thus the overall convergence is greatly accelerated. Improved convergence rates using the multigrid method, sometimes by as much as two orders of magnitudes, makes $f_R$ cosmological simulations a reality.

As shown in Fig. 7, convergence to a reasonable error tolerance takes ~1000 s on an AMD Opteron 2220 processor even for a modest $N_g = 256$ resolution. The FAS scheme has one of the best computation time scaling, growing linearly to the number of grid points (FFT, for comparison, scales as $N \log N$), and thus a $N_g = 512$ simulation will converge in 10 000 s. The $f_R$ field equation must be solved for each individual time step of the simulation, and thus resulting in potentially thousands of multigrid solutions totaling a few million seconds of CPU time. With our discretization scheme, we find that the simulation code spends ~95% of CPU time solving for the $f_R$ field. Such a percentage is at best a rough estimate, as the number of multigrid iterations required for convergence depends on the setup of the simulations.

Fortunately, several methods to speed up the simulation are possible. First, the particle positions between successive time steps does not change greatly, and thus the $f_R$ solution should not change significantly as well. The $f_R$ field solution from the previous time step provides a good initial guess for the iterative solver and we find that it results in ~10% faster convergence. Second, the FAS scheme is easily parallelized using shared memory parallelization with almost perfect scaling with the number of processor cores available. The NGS smoothing used extensively within the FAS scheme can be arranged in the so-called red-black ordering [26], such that smoothing of one particular grid point is independent of all other points except for its six nearest neighbors. This locality allows the smoothing to be split into local domains, each of which can be computed on separate processors. Combining such acceleration methods, a typical $N_g = 512$ simulation can be carried out in roughly 10 days on our hardware. We see no difficulties in extending the parallelism to distributed memory, although we have not implemented such an extension.

The memory requirement for the FAS scheme can be high compared to traditional PM simulations. The hierarchy of coarser grids adds $\sim$15% to the storage requirement for the $f_R$ field compared to the normal storage requirement for a 3D grid scaling as $N_g^3$. Furthermore, in order to accelerate the computation, we store the current residual error and use one additional grid hierarchy of the same size for transient computations. For a $N_g = 512$ grid, the required memory for our FAS implementation is $\sim$3.5 GiB using double precision floating point format (64 bits each). For comparison, storage of the density field requires 1 GiB, and the storage of dark matter particles requires 6 GiB for $512^3$ particles.

## V. RESULTS

In this section, we study a few $f_R$ simulations in order to highlight the differences between $f_R$ and ordinary $\Lambda$CDM physics. A more comprehensive study of the nonlinear $f_R$ physics is detailed in a companion paper [33].

### A. Two-body force laws

The first interesting case is the study of two-body force laws in $f_R$ cosmology. As is well known, in ordinary GR, two-body forces decay as $r^{-2}$ as the separation between the bodies, $r$, is varied. However, in $f_R$ cosmology, the new field mediates a fifth force that modifies two-body interactions and potentially changes the large scale structures of the Universe.

Such deviations from GR are easy to see using the same setup as the near point mass test in Sec. IV B. We solve for the peculiar gravitational potential, $\phi$, with the $f_R$ field and compute the gravitational acceleration at random positions in the simulation box, labeling them $g_{f(R)}$. In addition, we compute the standard Newtonian force using the inverse square law for the same set of points, labeling them $g_{\mathrm{Newton}}$. We use a $400h^{-1}$ Mpc computation box with $Ng = 256$, $\Omega_M = 0.3$, and $\Omega_\Lambda = 0.7$. Figure 8 shows the relative differences between $g_{f(R)}$ and $g_{\mathrm{Newton}}$ as a function of the distance away from the point mass. For strong $f_R$ fields, the gravitational forces near the central point mass are enhanced by as much as $\sim$30% over the unmodified forces. The range of the force enhancement is determined by the Compton wavelength of the $f_R$ field, which depends on the local field mass as

$$\lambda_{\mathrm{eff}} = m_{\mathrm{eff}}^{-1} \sim |f_R|^{(n+2)/2(n+1)}. \qquad (49)$$

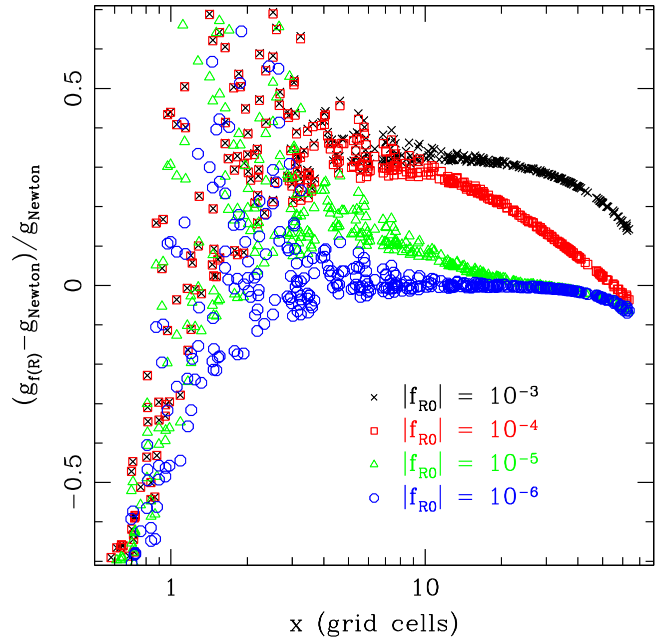


FIG. 8 (color online). Two-body acceleration as a function of separation for several $f_R$ field strengths. The accelerations are shown as relative differences from the exact Newtonian two-body acceleration. The large scatter at $x \sim 2$ is because of truncation errors resulting from differencing the potential at scales comparable to the grid size. At large radii from the center, the periodic boundary condition invalidates the comparison of forces in the simulation to those due to isolated two-body interactions. At such radii, the test particles are attracted to the neighboring periodic images of the central point mass.

Thus, the stronger the field, the farther out the gravitational enhancement of the $f_R$ field propagates, which is confirmed by Fig. 8. For the very weak field with $f_R = -10^{-6}$, the Compton wavelength is much smaller than the computational grid cells and therefore the gravitationally enhanced regions are not resolved.

In the strong field limit, the large Compton wavelength of the $f_R$ field makes it smooth and stiff, resisting the fluctuations in the underlying density field. Thus, in this limit, the deviation of the field, and hence of the curvature field $R$, vanishes and we have $\delta R \approx 0$. The equation for the gravitational potential, Eq. (17), reduces to

$$\nabla^2 \phi = \frac{16\pi G}{3}\delta\rho = \frac{4\pi}{3}\left(\frac{4}{3}G\right)\delta\rho. \qquad (50)$$

We see that the result is an effective enhancement of the Newton's constant by 33%, and hence the two-body forces enhanced by the same amount. Our two-body numerical solution captures this effect well, with the $f_{R0} = -10^{-3}$ acceleration curve plateauing at the correct value.

Features not due to the presence of the $f_R$ field are also seen in Fig. 8. The large scatter near $x \sim 2$ are due to the lack of force resolution at scales comparable to the underlying grid cells. At scales even smaller than the grid cells, computed forces vanish; this force decay is essential for the $N$-body system to remain collision free. On the other end of the scale, the periodic boundary condition begins to affect the forces as the test masses become gravitationally attracted to the neighboring point mass.

At first, Fig. 8 seems to contradict the stringent solar-system tests carried out so far and would constrain $f_R$ to very small values. However, the particular $f_R$ model chosen in this study shows the so-called chameleon behavior [13,14], in which the field strength is pushed to near zero in high density regions. Small-field strength in the high density region causes the effective field mass to increase and therefore the Compton wavelength to decrease. Thus, in our solar system, which sits in a relatively high density region of the Universe, the chameleon behavior may cause the $f_R$ field to be undetectable using our current technologies.

Our code is expected to reproduce this nonlinear chameleon behavior that is not incorporated into the linear analyses carried out so far. In order to investigate such effects, we place a spherical top hat of constant density at the center of a 200 Mpc simulation box. The sphere is 20 grid cells in radius, corresponding to 15.6 Mpc, and has a uniform overdensity of $\delta \sim 500$. Random test masses are placed both inside and outside the sphere, and the accelerations of the masses are calculated using the exact solution ($g_{\rm Newton}$) and $f_R$ simulations with various field strengths ($g_{f(R)}$). The exact solution of the acceleration increases linearly within the sphere and decreases as $r^{-2}$ outside the sphere.

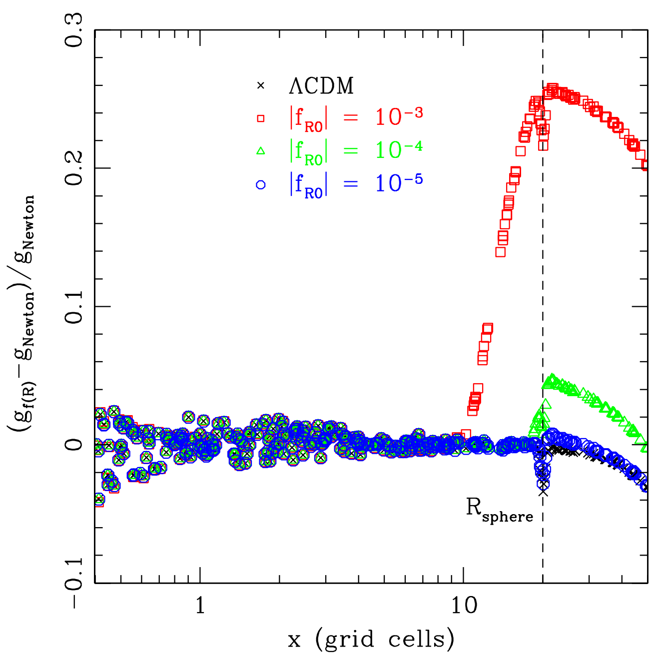


FIG. 9 (color online). Two-body acceleration as a function of separation for several $f_R$ field strengths. The spherical blob has a constant density of $\delta \sim 500$ and a radius of 20 grid cells ($15.6h^{-1}$ Mpc). The increased scatter in the accelerations at the surface of the sphere are due to the fact that a smoothness of the spherical surface is limited by the finite grid size of the simulation. As in Fig. 8, the acceleration field is affected by the periodic boundary condition at large radius.

In Fig. 9, we show the relative difference between $g_{f(R)}$ and $g_{\rm Newton}$ as a function of the separation between the center of the spherical blob and the test mass. Outside of the blob, the gravitational force is enhanced as expected from the results of Fig. 8. However, inside the blob, the $f_R$ field quickly dies down and the gravitational forces converge to that of ΛCDM. Strong $f_R$ fields can penetrate the density field farther, as seen in the case of $|f_R| = 10^{-3}$ that decays in $\sim 10h^{-1}$ Mpc.

### B. Revisiting the Zeldovich pancake

The Zeldovich 1D plane wave collapse offers insights into the differences in the particle dynamics in the presence of $f(R)$ modifications. We run three Zeldovich pancake simulations starting with the same cosmology and initial conditions as in Fig. 4 except for $f(R)$ modifications. In Fig. 10, we show the resulting difference in particle momenta relative to those of the unmodified GR simulation. Because of the fifth force due to $f_R$, the sine wave collapses faster as the field strength is increased. In addition, we see the effects of the finite range of the fifth force, which is determined by the Compton wavelength of the $f_R$ field, Eq. (49). In the case of weak field, $f_{R0} = -10^{-4}$, there is no significant enhancement in the particle momenta at distances greater than $\sim 10$ code units ($\sim 16h^{-1}$ Mpc)

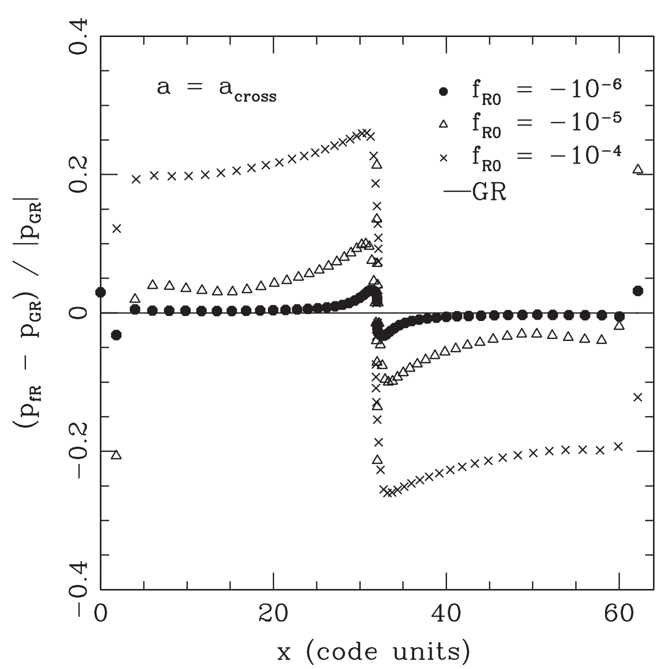


FIG. 10. The relative differences in particle momenta in Zeldovich pancake simulations with varying $f_R$ field strengths. The simulation snapshot is taken at $a = a_{\rm cross} = 1$.

away from the collapsed pancake, and the range of the fifth force is shown to be larger for stronger $f_R$ fields. For the strongest field, the fifth force does not decay sufficiently before the periodic image of the pancake starts to become important.

The Zeldovich collapses show no sign of the chameleon behavior, even for the weakest $f_R$ field. The pancake is essentially a sheet mass and thus does not have an *extended* region of high density. Therefore, the $f_R$ field does not appreciably decay near the pancake and no chameleon behavior is expected.

### C. Cosmological power spectrum

Finally, we apply our code to a realistic cosmological simulation in order to study the effects of the $f_R$ field to the large scale structures. We have run $f(R)$ cosmological simulations using the same setup as those found in Sec. IV C and with $f_{R0} = -10^{-5}$. The strength of the $f_R$ field is chosen to highlight the differences in the power spectra.

With our simulation setup having twice as many grid points as particles per one dimension, we find that at the initial redshift, some of the grid cells in the simulations have no particles nearby and therefore have zero density. At early redshifts, the cosmology is very nearly $\Lambda$CDM, and we have $R = 8\pi G\rho$. Thus, in the empty grid cells, the curvature is almost exactly zero and we have a formal divergence of the $f_R$ field in such grid cells. The particle dynamics, however, is governed by the peculiar potential, and therefore by the curvature and density fields, not directly by the $f_R$ field [see Eq. (28)]. We have checked that our potential solver and particle trajectory integrators remain stable and accurate even when such divergences are present (see Fig. 3). At late times, we also find empty grid cells within large voids. However, the mean Compton wavelength of the $f_R$ field becomes sufficiently large and smooths out the $f_R$ field, thereby avoiding any potential divergences in the field at late times.

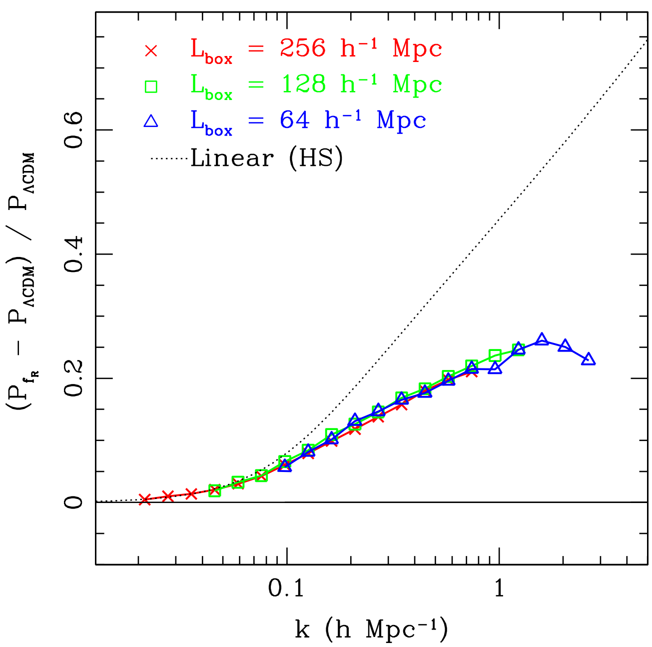


FIG. 11 (color online). Relative differences between the power spectra of $|f_{R0}| = 10^{-5}$ simulations and unmodified $\Lambda$CDM simulations. The linear prediction is taken from Hu and Sawicki [12] and assumes no chameleon behavior. The power spectra for each box size are only plotted up to their respective half-Nyquist wave numbers, which are $0.79h$ Mpc$^{-1}$, $1.57h$ Mpc$^{-1}$, and $3.14h$ Mpc$^{-1}$ for L256, L128, and L64 simulations, respectively.

Figure 11 shows the relative differences between the power spectra with and without $f(R)$ modifications, along with the linear prediction for the power spectrum enhancement taken from [12]. The linear prediction assumes no chameleon behavior and thus is expected to overestimate the power spectrum enhancement when there is strong suppression of the $f_R$ field in high density regions. The simulated power spectra match the linear predictions at large scales, where nonlinear effects, such as the chameleon mechanism, are expected to be negligible. The smallest simulation box, $L_{\rm box} = 64h^{-1}$ Mpc, does not have sufficient statistics to accurately represent the largest modes. At scales smaller than $k \sim 0.1h$ Mpc, we see a striking deviation of the simulations from the linear prediction, showing clear signs the previously unquantified effects of nonlinear $f(R)$ physics.

A more detailed comparison of the power spectra are carried out in the companion paper.

## VI. CONCLUSION

In this paper, we have introduced a method to construct a cosmological $N$-body simulation with a class of viable $f(R)$ modifications to general relativity. Our simulation code, implemented in standard C++, solves the HS model of $f(R)$ modification using the particle-mesh method, particularly suited because the scalar degree of freedom in the model is well represented as a scalar field (i.e., a mesh) coupled to the Newtonian potential. The nonlinear field equation for $f_R$ is solved on the mesh using an efficient multigrid scheme that is shown to converge robustly to the desired solution. The code is also shown to reproduce the chameleon behavior of the HS model.

The code should allow us to gain insight into the quasi-nonliear physics of $f(R)$ modified gravity models. In general, gravitational forces are enhanced under the HS model, and we show that the resulting power spectra are also enhanced compared to the $\Lambda$CDM power spectrum. We further show hints that the power spectrum enhancement is smaller than the linear predictions due to the chameleon mechanism that has not so far been modeled. In a companion paper [33], we further study the effects of the HS model on the dark matter power spectrum and its cosmological implications. In addition, effects on the cluster mass function and weak lensing statistics are potentially interesting and should be investigated in the future.

Lastly, the work presented here can be used as a general framework for nonlinear simulation of any minimally coupled scalar field model of gravity, provided that the resulting field equations are sufficiently stable under relaxation and multigrid schemes. In particular, an interesting exercise might be to apply this framework to the Dvali, Gabadadze, and Porrati (DGP) model [34].

## ACKNOWLEDGMENTS

We would like to thank Wayne Hu, Marcos Lima, Justin Khoury, Josh Frieman, and Jeremy Tinker for insightful and useful discussions and Andrey Kravtsov for guiding the authors during the implementation and testing of the simulation code. This work was supported in part by the Kavli Institute for Cosmological Physics (KICP) at the University of Chicago through NSF Grants No. PHY-0114422 and No. PHY-0551142 and an endowment from the Kavli Foundation and its founder Fred Kavli. H. O. was additionally supported by the NSF Grants No. AST-0239759, No. AST-0507666, and No. AST-0708154 at the University of Chicago. Some of the computations used in this work have been performed on the Joint Fermilab—KICP Supercomputing Cluster, supported by grants from Fermilab, Kavli Insititute for Cosmological Physics, and the University of Chicago. This research has made use of NASA's Astrophysics Data System and the arXiv.org preprint service funded by Cornell University and the NSF.

## APPENDIX A: DETAILS OF THE DISCRETIZATION

In our implementation, Eq. (34) is discretized much like a standard variable coefficient Poisson equation. We let $a = e^u$, $a_{i+(1/2),j,k} = (a_{j,j,k} + a_{j+1,j,k})/2$, and $a_{i-(1/2),j,k} = (a_{i,j,k} + a_{i-1,j,k})/2$. Then, we have

$$\begin{aligned}\mathcal{L} = {}& \frac{1}{h^2}(a_{i-(1/2),j,k}u_{i-1,j,k} - (a_{i-(1/2),j,k} + a_{i+(1/2),j,k})u_{i,j,k} + a_{i+(1/2),j,k}u_{i+1,j,k}) + \frac{1}{h^2}(a_{i,j-(1/2),k}u_{i,j-1,k} \\ & - (a_{i,j-(1/2),k} + a_{i,j+(1/2),k})u_{i,j,k} + a_{i,j+(1/2),k}u_{i,j+1,k}) + \frac{1}{h^2}(a_{i,j,k-(1/2)}u_{i,j,k-1} - (a_{i,j,k-(1/2)} + a_{i,j,k+(1/2)})u_{i,j,k} \\ & + a_{i,j,k+(1/2)}u_{i,j,k+1}) - \frac{\Omega_{\mathrm{M},0}}{a\tilde{c}^2\bar{f}_R}\left[\frac{R(\bar{f}_R e^{u}_{i,j,k}) - \bar{R}}{3} - \delta_{i,j,k}\right]. \end{aligned} \tag{A1}$$

We find that the above discretization performs better than discretizing the equation after expanding out the derivative operators. Even using this discretization, we find that the iterations can diverge if the initial guess is sufficiently poor. We find that using variable, and often smaller, Newton-Raphson step sizes (i.e., successive *under*-relaxation) can effectively avoid such divergences until the trial solution is sufficiently close to the true solution.

## APPENDIX B: FAS IMPLEMENTATION

In our FAS implementation, we use the full-weighting restriction operator ($I_h^{2h}$) and the bilinear interpolation operator ($I_{2h}^h$) for prolongation. The full-weighting operator, in 3D, is given by

$$u^{2h}_{i,j,k} = \sum_{\alpha,\beta,\gamma=-1}^{1} \sigma_{\alpha,\beta,\gamma} u^h_{2i+\alpha,2j+\beta,2k+\gamma}, \tag{B1}$$

where

$$\begin{aligned} \sigma_{\alpha,\beta,\gamma} &= \tfrac{1}{8} \quad \text{if } |\alpha| + |\beta| + |\gamma| = 0, \\ \sigma_{\alpha,\beta,\gamma} &= \tfrac{1}{16} \quad \text{if } |\alpha| + |\beta| + |\gamma| = 1, \\ \sigma_{\alpha,\beta,\gamma} &= \tfrac{1}{32} \quad \text{if } |\alpha| + |\beta| + |\gamma| = 2, \\ \sigma_{\alpha,\beta,\gamma} &= \tfrac{1}{64} \quad \text{if } |\alpha| + |\beta| + |\gamma| = 3. \end{aligned}$$

Note that the $2h$ superscript denotes a variable defined on the coarse grid (i.e., a grid with spacing of $2h$) and the $h$ superscript denotes a variable defined on the fine grid. The bilinear interpolation operator is given by

$$\begin{aligned} u^h_{2i,2j,2k} &= u^{2h}_{i,j,k}, \\ u^h_{2i+1,2j,2k} &= \tfrac{1}{2}(u^{2h}_{i,j,k} + u^{2h}_{i+1,j,k}), \\ u^h_{2i,2j+1,2k} &= \tfrac{1}{2}(u^{2h}_{i,j,k} + u^{2h}_{i,j+1,k}), \\ u^h_{2i,2j,2k+1} &= \tfrac{1}{2}(u^{2h}_{i,j,k} + u^{2h}_{i,j,k+1}), \\ u^h_{2i+1,2j+1,2k} &= \tfrac{1}{4}(u^{2h}_{i,j,k} + u^{2h}_{i+1,j,k} + u^{2h}_{i,j+1,k} + u^{2h}_{i+1,j+1,k}), \\ u^h_{2i,2j+1,2k+1} &= \tfrac{1}{4}(u^{2h}_{i,j,k} + u^{2h}_{i,j+1,k} + u^{2h}_{i,j,k+1} + u^{2h}_{i,j+1,k+1}), \\ u^h_{2i+1,2j,2k+1} &= \tfrac{1}{4}(u^{2h}_{i,j,k} + u^{2h}_{i+1,j,k} + u^{2h}_{i,j,k+1} + u^{2h}_{i+1,j,k+1}), \\ u^h_{2i+1,2j+1,2k+1} &= \tfrac{1}{8}(u^{2h}_{i,j,k} + u^{2h}_{i+1,j,k} + u^{2h}_{i,j+1,k} + u^{2h}_{i,j,k+1} \\ &\quad + u^{2h}_{i+1,j+1,k} + u^{2h}_{i+1,j,k+1} + u^{2h}_{i,j+1,k+1} \\ &\quad + u^{2h}_{i+1,j+1,k+1}). \end{aligned} \tag{B2}$$

Other choices of restriction and prolongation operators are certainly possible. However, we find that the above choices result in the fastest and most stable FAS implementation for this particular problem.

[1] J. Frieman, M. Turner, and D. Huterer, arXiv:0803.0982.
[2] S. M. Carroll, V. Duvvuri, M. Trodden, and M. S. Turner, Phys. Rev. D **70**, 043528 (2004).
[3] S. Nojiri and S. D. Odintsov, Phys. Rev. D **68**, 123512 (2003).
[4] S. Capozziello, S. Carloni, and A. Troisi, Recent Res. Dev. Astron. Astrophys. **1**, 625 (2003).
[5] J. G. Williams, X. X. Newhall, and J. O. Dickey, Phys. Rev. D **53**, 6730 (1996).
[6] J. D. Anderson, P. A. Laing, E. L. Lau, A. S. Liu, M. M. Nieto, and S. G. Turyshev, Phys. Rev. Lett. **81**, 2858 (1998).
[7] B. Bertotti, L. Iess, and P. Tortora, Nature (London) **425**, 374 (2003).
[8] J. G. Williams, S. G. Turyshev, and D. H. Boggs, Phys. Rev. Lett. **93**, 261101 (2004).
[9] R. A. Knop, G. Aldering, R. Amanullah, P. Astier, G. Blanc, M. S. Burns, A. Conley, S. E. Deustua, M. Doi, R. Ellis *et al.*, Astrophys. J. **598**, 102 (2003).
[10] A. G. Riess, L.-G. Strolger, J. Tonry, S. Casertano, H. C. Ferguson, B. Mobasher, P. Challis, A. V. Filippenko, S. Jha, W. Li *et al.*, Astrophys. J. **607**, 665 (2004).
[11] D. N. Spergel, R. Bean, O. Doré, M. R. Nolta, C. L. Bennett, J. Dunkley, G. Hinshaw, N. Jarosik, E. Komatsu, L. Page *et al.*, Astrophys. J. Suppl. Ser. **170**, 377 (2007).
[12] W. Hu and I. Sawicki, Phys. Rev. D **76**, 064004 (2007).
[13] J. Khoury and A. Weltman, Phys. Rev. D **69**, 044026 (2004).
[14] J. Khoury and A. Weltman, Phys. Rev. Lett. **93**, 171104 (2004).
[15] Y.-S. Song, W. Hu, and I. Sawicki, Phys. Rev. D **75**, 044004 (2007).
[16] L. Pogosian and A. Silvestri, Phys. Rev. D **77**, 023503 (2008).
[17] W. Hu and I. Sawicki, Phys. Rev. D **76**, 104043 (2007).
[18] T. P. Sotiriou and V. Faraoni, arXiv:0805.1726.
[19] Y.-S. Song, H. Peiris, and W. Hu, Phys. Rev. D **76**, 063517 (2007).
[20] R. W. Hockney and J. W. Eastwood, *Computer Simulation Using Particles* (McGraw-Hill, New York, 1981).
[21] E. Bertschinger, Annu. Rev. Astron. Astrophys. **36**, 599 (1998).
[22] S. F. Shandarin, Astrophysics (Engl. Transl.) **16**, 439 (1981).
[23] A. V. Kravtsov, A. A. Klypin, and A. M. Khokhlov, Astrophys. J. Suppl. Ser. **111**, 73 (1997).
[24] W. H. Press, S. A. Teukolsky, W. T. Vetterling, and B. P. Flannery, *Numerical Recipes in C. The Art of Scientific Computing* (Cambridge University Press, Cambridge, England, 1992), 2nd ed.
[25] A. Brandt, *Proceedings of the Third International Conference on Numerical Methods in Fluid Mechanics*, edited by H. Cabannes and R. Temam, Lecture Notes in Physics Vol. 18 (Springer-Verlag, Berlin, 1973), p. 82.
[26] W. L. Briggs, V. E. Henson, and S. F. McCormick, *A Multigrid Tutorial* (Society for Industrial and Applied Mathematics, Philadelphia, 2000), 2nd ed., ISBN 0-89871-462-1.
[27] A. Klypin and J. Holtzman, arXiv:astro-ph/9712217.
[28] A. A. Klypin and S. F. Shandarin, Mon. Not. R. Astron. Soc. **204**, 891 (1983).
[29] G. Efstathiou, M. Davis, S. D. M. White, and C. S. Frenk, Astrophys. J. Suppl. Ser. **57**, 241 (1985).
[30] R. E. Smith, J. A. Peacock, A. Jenkins, S. D. M. White, C. S. Frenk, F. R. Pearce, P. A. Thomas, G. Efstathiou, and H. M. P. Couchman, Mon. Not. R. Astron. Soc. **341**, 1311 (2003).
[31] B. W. O'Shea, G. Bryan, J. Bordner, M. L. Norman, T. Abel, R. Harkness, and A. Kritsuk, arXiv:astro-ph/0403044.
[32] D. J. Eisenstein and W. Hu, Astrophys. J. **496**, 605 (1998).
[33] H. Oyaizu, M. Lima, and W. Hu, following Article, Phys. Rev. D **78**, 123524 (2008).
[34] G. Dvali, G. Gabadadze, and M. Porrati, Phys. Lett. B **485**, 208 (2000).